

A new synchrotron rapid-scanning X-ray fluorescence (SRS-XRF) imaging station at SSRL beamline 6-2

Nicholas P. Edwards,^{a*} Samuel M. Webb,^a Courtney M. Krest,^a Douglas van Campen,^a Phillip L. Manning,^b Roy A. Wogelius^c and Uwe Bergmann^{d*}

Received 7 April 2018

Accepted 14 July 2018

Edited by I. Lindau, SLAC/Stanford University, USA

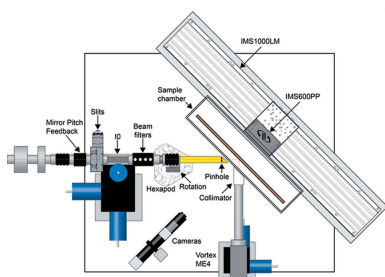
Keywords: synchrotron; X-ray; fossils; fluorescence; imaging.

^aStanford Synchrotron Radiation Lightsource, SLAC National Accelerator Laboratory, 2575 Sand Hill Road, Menlo Park, CA 94025, USA, ^bSchool of Earth and Environmental Science, Interdisciplinary Centre for Ancient Life, University of Manchester, Manchester M13 9PL, UK, ^cSchool of Earth and Environmental Science, Williamson Research Centre for Molecular Environmental Science, University of Manchester, Manchester M13 9PL, UK, and ^dStanford PULSE Institute, SLAC National Accelerator Laboratory, Menlo Park, CA 94025, USA.
*Correspondence e-mail: nicholas.edwards@slac.stanford.edu, bergmann@slac.stanford.edu

This paper describes a new large-range rapid-scan X-ray fluorescence (XRF) imaging station at beamline 6-2 at the Stanford Synchrotron Radiation Lightsource at SLAC National Accelerator Laboratory. This station uses a continuous rapid-scan system with a scan range of 1000×600 mm and a load capacity of up to 25 kg, capable of 25–100 μm resolution elemental XRF mapping and X-ray absorption spectroscopy (XAS) of a wide range of objects. XRF is measured using a four-element Hitachi Vortex ME4 silicon drift detector coupled to a Quantum Detectors Xspress3 multi-channel analyzer system. A custom system allows the X-ray spot size to be changed quickly and easily *via* pinholes ranging from 25 to 100 μm , and the use of a poly-capillary or axially symmetric achromatic optic may achieve a <10 μm resolution in the future. The instrument is located at wiggler beamline 6-2 which has an energy range of 2.1–17 keV, creating *K* emission for elements up to strontium, and *L* or *M* emission for all other elements. XAS can also be performed at selected sample positions within the same experiment, allowing for a more detailed chemical characterization of the elements of interest. Furthermore, sparse excitation energy XRF imaging can be performed over a wide range of incident X-ray energies. User friendliness has been emphasized in all stages of the experiment, including versatile sample mounts, He purged chambers for low-*Z* analyses, and intuitive visualization hardware and software. The station provides analysis capabilities for a wide range of materials and research fields including biological, chemical, environmental and materials science, paleontology, geology and cultural heritage.

1. Introduction

Synchrotron-based X-ray fluorescence (XRF) imaging is a powerful analytical tool that has been applied in a wide range of scientific fields including life sciences (*e.g.* Suortti & Thomlinson, 2003; Korbas *et al.*, 2008; Popescu *et al.*, 2009; Punshon *et al.*, 2009), archaeology and cultural heritage (*e.g.* Dooryh e *et al.*, 2004; Sandstr om *et al.*, 2005; Bergmann, 2007, 2012; Bertrand *et al.*, 2012; Janssens *et al.*, 2013; Zielińska *et al.*, 2013), environmental and earth sciences, and paleontology (*e.g.* Brown & Sturchio, 2002; Templeton & Knowles, 2009; Bergmann *et al.*, 2010; Edwards *et al.*, 2014; Johnson *et al.*, 2016; Gueriau *et al.*, 2018). Although laboratory/benchtop XRF analytical systems have practical and cost advantages, synchrotron radiation provides several performance advantages related to its high brightness, tunable energy and



polarization of the X-rays (Winick, 1994; Wiedemann, 2003; Aquilanti *et al.*, 2015). The benefits are of particular importance for XRF imaging and include higher spatial resolution, scanning speed, greater sensitivity to trace elements and improved signal to noise ratio (as scattering can be suppressed and the incident energy can be optimized for a given element). Another benefit that is critical for some applications is the ability to perform X-ray absorption spectroscopy (XAS) analysis to acquire chemical speciation information.

Modern advances in detectors and signal processors have considerably improved data acquisition rates, allowing for rapid and continuous scanning of samples with pixel dwell times in the millisecond and lower range (Vogt & Lanzirotti, 2013; Kempson *et al.*, 2014; Barkan *et al.*, 2015; Lanzirotti *et al.*, 2016; Diaz-Moreno *et al.*, 2018). Various approaches to these systems are available around the globe such as the large area detector (Maia) employed at the Australian Synchrotron (Kirkham *et al.*, 2010; Paterson *et al.*, 2011). The main advantage of these large area detectors is the solid angle, the main disadvantage being the poorer spectral resolution for the XRF analysis and larger scattering background, as these detectors are placed in a back-scattering geometry. Whether one system is more suited than another has to be decided on a case-by-case basis.

These systems have enabled XRF beamlines to produce megapixel images on a micrometer scale (Vogt & Lanzirotti, 2013; Lanzirotti *et al.*, 2016). Most beamline development has focused on XRF microscopy of very small samples and therefore have pushed the development of technology to support sub-micrometer spatial resolution, and commercial systems are becoming available to scan much larger objects (paintings for example) with a higher spatial resolution in the range 10–500 μm [e.g. Bruker M6 Jetstream (Bruker Corporation; <https://www.bruker.com/products/x-ray-diffraction-and-elemental-analysis/micro-xrf-and-txrf/m6-jetstream/technical-details.html>) and Sigray AttoMap (Sigray Inc.; <http://www.sigray.com/attomap>)]. However, samples that are tens of centimeters in length and height bring a unique set of practical issues with mechanical and logistical requirements that are typically not compatible with microfocus applications. In order to maintain sub-micrometer precision, typical micrometer-scanning systems are not designed to analyze large and heavy samples. Furthermore, many experimental hutches at synchrotrons are limited in space or sample environments that permit the freedom of movement of large objects. Ideally, one would like to be able to analyze large and heavy objects with a spatial resolution ranging from $\sim 100 \mu\text{m}$ for maps of the full object to a few micrometers for select areas. The instrument described here is optimized for this task.

During the last decade, a large-range XRF imaging instrument, which was originally designed for rapid-scan XRF imaging of the Archimedes Palimpsest (Bergmann, 2007), has been operational at the Stanford Synchrotron Radiation Lightsource (SSRL, CA, USA) beamline 6-2. Over the years this instrument has been extensively applied in the field of archaeology, medical imaging, geology and paleontology (e.g. Popescu *et al.*, 2009; Bergmann *et al.*, 2010, 2012; Wogelius *et*

al., 2011; Anné *et al.*, 2014, 2016, 2017; Edwards *et al.*, 2014, 2016; Egerton *et al.*, 2015; Harazim *et al.*, 2015). However, despite the fact that this instrument has been continuously modified over the years, development was limited by the existing hardware and software.

Here we describe a new synchrotron rapid-scanning XRF (SRS-XRF) instrument that is now in the commissioning phase at SSRL beamline 6-2. This instrument provides the community with a user-friendly and flexible rapid-scan XRF imaging station based on state-of-the-art alignment, scanning, detection and data acquisition/processing instrumentation. Beamline 6-2 spans the energy range 2.1–17 keV, allowing for tender to hard X-ray experiments. The instrument is capable of rapid XRF imaging of very large samples up to $1000 \times 600 \text{ mm}$ in size with a load capacity of $\sim 25 \text{ kg}$, and yet has sub-micrometer scanning precision and repeatability. In addition to rapidly imaging large areas, smaller regions of interest can be targeted for a more detailed analysis at higher spatial resolution without the need for remounting or sub-sampling parts of the larger specimen with a readily changeable beam spot size (described below). This will be especially beneficial for the study of rare and precious objects which have short time frames for access and often cannot be sampled or remounted. The technical details and examples demonstrating the performance of this operational end-station are presented below.

2. Technical description

The imaging station is located at the 56-pole (55 full-strength and 2 end poles) 0.9 T wiggler beamline 6-2 at SSRL (Fig. 1*a*). Beamline 6-2 is equipped with two liquid-nitrogen-cooled double-crystal monochromators, Si(111) and a Si(311), that can be alternately operated depending on the required energy resolution (Sokaras *et al.*, 2013). The X-ray experiments discussed here are operated using the Si(111) monochromator. Collimating and double-focusing Rh-coated mirrors are positioned before (M0) and after (M1) the monochromator, respectively. Nominal pitch for M0 is 3.75–6.8 mrad, and for M1 is 3.75–4.95 mrad.

The beamline delivers monochromatic X-rays over an energy range of 2.1–17 keV, which allows for experiments to be performed in both ‘high-*Z*’ (optimized for Ca–Sr *K*-emission XRF imaging) and ‘low-*Z*’ (optimized for Al–Cl *K*-emission XRF imaging and S XAS) setups, under the current SPEAR3 storage ring operational conditions at an electron energy of 3 GeV and 500 mA current in top-off mode. Optimum photon flux into the hutch is $\sim 1 \times 10^{13} \text{ photons s}^{-1}$ at 6.5 keV with an energy resolution of $\sim 850 \text{ meV}$ transmitted through the Si(111) monochromator (Sokaras *et al.*, 2013). At 13.5 keV, flux is $\sim 7 \times 10^{12} \text{ photons s}^{-1}$ and at 3.15 keV is $\sim 3 \times 10^{11} \text{ photons s}^{-1}$. The beam can be focused to a size of approximately $150 \mu\text{m} \times 400 \mu\text{m}$ full width at half-maximum (FWHM) at the pinhole position. Photon flux on the sample is correspondingly reduced depending on the size of the pinhole. For example, flux through a $50 \mu\text{m}$ pinhole is typically between

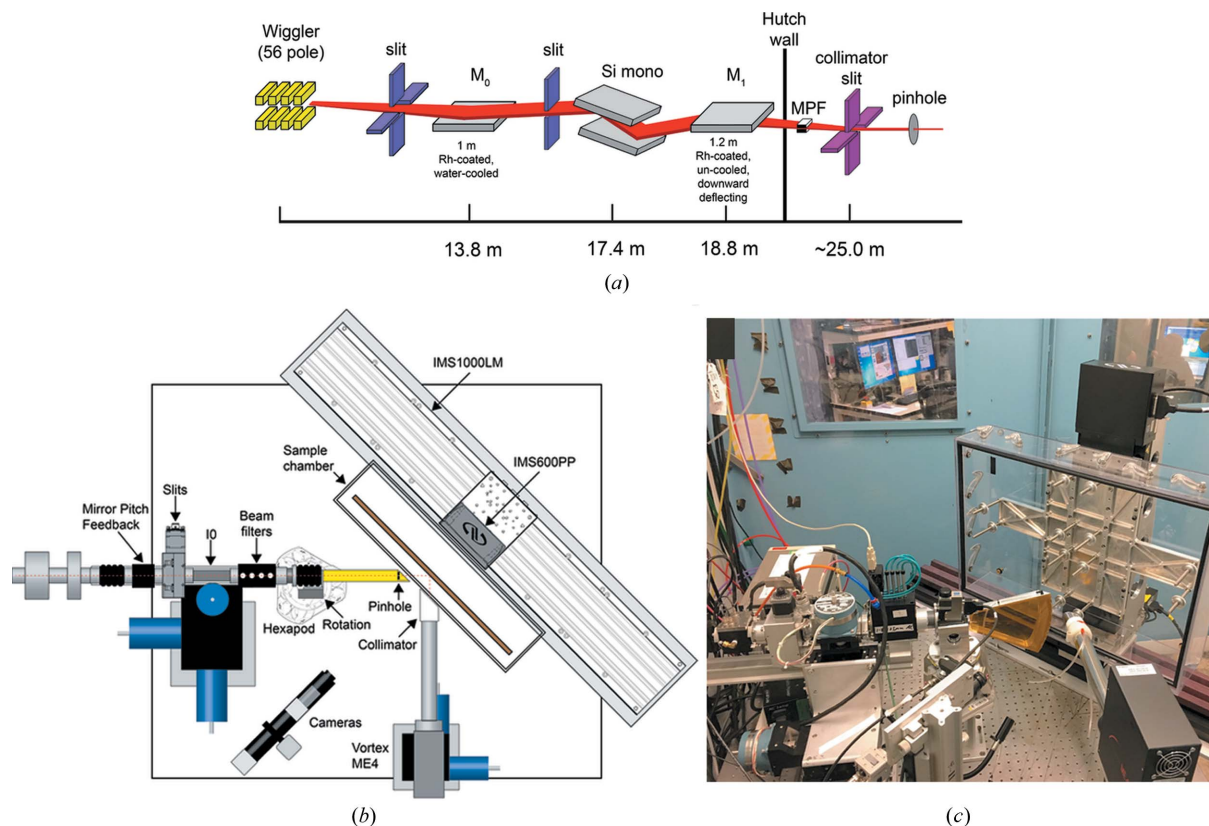


Figure 1

(a) Beamline 6-2 schematic (not to scale). (b) Plan-view schematic (to scale) and (c) photograph of the rapid imaging system as it is currently operated at SSRL beamline 6-2. Note that the vertical stage shown is an IMS300PP (30 cm travel); the custom IMS600PP (60 cm travel) was not installed at the time this image was taken.

10^{10} and 10^{11} photons s^{-1} at 13.5 keV, and between $\sim 10^9$ and 10^{10} photons s^{-1} at 3.15 keV.

A plan-view schematic of the XRF imaging system is presented in Fig. 1(b). The beam enters the hutch and passes through a mirror pitch feedback system that maintains beam stability, limiting beam drift with SPEAR3 cycles. The beam then passes through a set of slits (JJ X-ray IB-C30-AIR), an ion chamber (IO) and a filter box integrated into the mapping software to provide automatic shutter control for delicate samples. At the beam pipe exit, there is a pinhole assembly for controlling beam spot size (discussed below). The sample is rastered relative to the incident X-ray beam by being mounted on precision (sub-micrometer accuracy and repeatability) encoded motorized linear motion stages. Three stages are combined to provide three axes of motion: horizontal [Newport IMS1000LM (<https://www.newport.com/p/M-IMS1000LM>)], vertical [a customized IMS600PP (<https://www.newport.com/p/IMS600PP>)] and depth (for motion perpendicular to the horizontal and scanning direction). These have 1000 mm, 600 mm and 100 mm of travel, respectively, providing an effective 1000 mm \times 600 mm scanning area and enabling the depth alignment of samples with different thicknesses. The vertical 600 mm travel stage, on which the sample is mounted, has been customized to achieve a 25 kg total load capacity (sample environment and sample). For example, for a 50 mm-thick slab of average density rock (2.65 g cm^{-3}), this would enable a slab $\sim 400 \text{ mm} \times 400 \text{ mm}$ to

be analyzed. In standard scanning operation, the continuous movement is horizontal with a vertical step at the end of each line. Stage motion is controlled by a Newport XPS-Q6 controller (<https://www.newport.com/f/xps-universal-multi-axis-motion-controller>). The sample and horizontal motion is set at 45° angle to the incident beam. XRF is measured using a four-element Vortex ME4 silicon drift diode detector (Hitachi Inc; http://www.hitachi-hightech.com/hhs-us/product_detail/?pn) positioned at 90° to the incident beam and 45° to the sample surface in order to minimize scattering.

The incident and transmission ion chambers of the beamline (IO and I1, respectively) are connected to SRS-570 (Stanford Research Systems) current-voltage amplifiers, using a high-bandwidth setting for the fastest response time. The voltages are sent to a high-speed V2F converter [V2F100 (Quantum Detectors; <http://quantumdetectors.com/n/products/v2f100-100-mhz-v2f-converter>)] which has a maximum pulse rate of 100 MHz. These pulses are counted by the Zebra (Quantum Detectors; <http://quantumdetectors.com/zebra/>) process and acquisition system, which also controls the various gate pulses required to gate the detector system. The ME4 is coupled to an Xspress3 multi-channel analyzer system (Quantum Detectors; <http://quantumdetectors.com/xspress3/>) providing an energy resolution of $\sim 150 \text{ eV}$. The Xspress3 performs the detector signal pulse processing and provides a usable count rate of up to 3×10^6 counts s^{-1} per detector element, while maintaining the detector energy resolution. This key

improvement removes one of the most serious bottlenecks at the readout stage required for rapid-scanning applications. The Xspress3 system is triggered at each pixel by pulses generated by the Newport XPS motor controller. The XPS controller sends gate pulses *via* the position compare output (PCO) port, within a defined region on the sample at the desired pixel size. As the stage is continuously scanned across the X-ray beam, the XPS pulses are processed to the Zebra and Xspress3 systems ensuring that all pixels have the same gating pulse for both ion chamber and fluorescence detection. Any irregularities in the travel of the stage (*i.e.* acceleration, deceleration, oscillations in velocity) are accurately measured at each pixel at the resolution of the Xspress3 clock (~ 12.5 ns) which also ensures that all data rows are aligned during analysis.

Another key improvement over the previous instrument is the acquisition of a full XRF spectrum for every image pixel in addition to up to 16 user-defined windowed elements. When combined with the appropriate calibration, this enables peak fitting that allows for a more accurate element-distribution analysis and quantification. Furthermore, elements not windowed during the experiments can be analyzed if needed after finishing the scan. This allows manipulation of the full XRF spectrum for redisplay with no need to rescan the sample, which can be critical if, for example, a new element of interest is discovered or for radiation-sensitive samples which cannot be analyzed multiple times. Finally, data are saved at the end of each line allowing up to 16 elemental maps to be displayed and interrogated while the analysis progresses. This allows for fast feedback and thus improves the efficient use of the beam-time allocation and optimizes data acquisition for each scan.

Sample visualization, alignment and efficient setup of scanning areas is another important improvement that has been implemented in this new instrument. Two cameras provide a live video feed of the sample: a fixed wide-angle digital video camera provides ~ 350 mm-wide field of view and a Navitar 12 \times Zoom microscope/camera system provides higher magnification from 40 mm to 5 mm-wide views. The video is fed to the mapping GUI and this feed is calibrated to the stage movement so that map regions can be drawn directly on the live camera image. Map parameters are automatically populated and step size and dwell time can be user defined. Once all the map parameters have been defined, the software performs all the necessary calculations to carry out the experiment and provide a scan time estimate. This update is a major improvement over the previous system that required manual calculations for each change in map size and count time.

3. Beam spot size

One of the primary advantages of large-scale imaging is the ability to use the centimeter- and decimeter-scale elemental distributions to target areas

of interest for higher-resolution imaging or analysis *via* other methods. Normally, acquiring large map (decimeter scale) areas in a reasonable amount of time requires relatively large spot sizes. Acquiring higher-resolution (<10 μm) data is also highly desirable (especially for heterogeneous samples), as shown by the variety and abundance of microfocus and nanometer-resolution techniques available. However, to perform analyses at both scales would normally require a sample to be analyzed at a different beamline, on a different scanning stage or *via* another technique optimized for such high spatial resolutions. This can be very impractical as it requires a move, remounting, realignment or sub-sampling of sometimes very precious samples which is often not possible. As such, there is a need for the ability to switch beam spot sizes simply and quickly during the same experiment. Being able to rapidly change the beam spot size over several orders of magnitude allows for greater flexibility and this large spatial dynamic range enables completion of a full specimen analysis in one beam session. This feature is particularly important for rare and valuable specimens with limited access.

The scanning stages on this new instrument have the required sub-micrometer resolution, and for reproducibly changing pinholes we have developed a system that consists of a rotational stage attached to a six-axis hexapod [Newport HXP50-MECA (<https://www.newport.com/p/HXP50-MECA>) and ELEC (Newport Corporation; <https://www.newport.com/p/HXP50-ELEC>)]. Attached to the rotation stage is an assembly that currently holds a series of tungsten pinholes (100, 50, 35 and 25 μm diameter) (Fig. 2). The rotation stage performs the coarse movement to bring the requested pinhole into the path of the incident beam, and the hexapod is then used for fine-scale alignment. Alignment for each optic is performed and pre-set by the beamline scientist prior to the start of an experiment. The user then simply has to select the desired pinhole size with the GUI and the assembly automatically rotates to the requested pinhole and sets the appropriate hexapod position. Should alignment be lost, a scanning program (which is already in place) can scan the pinhole position against the ion chamber or fluorescence intensities through multiple axes, providing clear and simple visualization of the optimum alignment position, allowing users to easily re-acquire optimum beam intensity. Furthermore, for lower-energy experiments (below 3500 eV), this

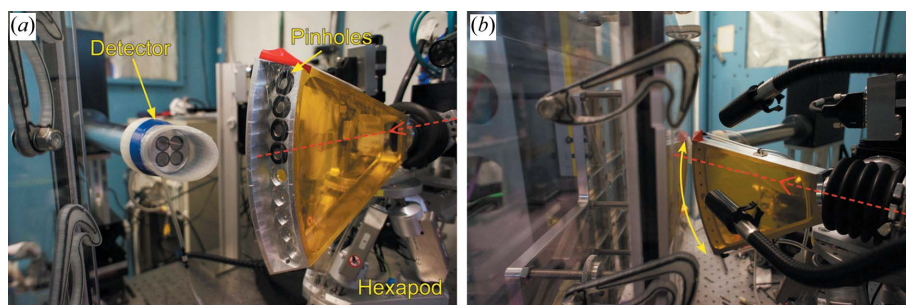


Figure 2 Photographs of the pinhole assembly and Vortex detector with its snout collimator. Dashed lines show the incident beam path and the curved arrow indicates rotational movement of the assembly.

pinhole assembly has been designed to situate the pinholes as close to the sample surface as practically possible and is He purged to minimize absorption by air. Although we are currently using 25–100 μm W pinholes, the use of a polycapillary or axially symmetric achromatic optic may allow us to achieve $<10\ \mu\text{m}$ resolution in the future. For reference, flux does not scale linearly with pinhole size because of the Gaussian profile of the beam. The pinhole area increases by approximately two times between the 25 μm and 35 μm pinhole, and the 35 μm and 50 μm pinhole, while the recorded transmitted flux values increase by factors of ~ 2.31 and ~ 1.67 , respectively. Finally, inherent beam divergence results in a slightly larger beam spot size incident on the sample than that defined by the pinhole. Pinhole-to-sample distance is a significant factor in defining spot size. Based on the current operating parameters with a pinhole to sample distance of 3–5 cm, we calculate (at worst) that a 100 μm pinhole will produce a spot size on the sample that is 15–25% larger, and a 25 μm pinhole will produce a spot size 45–75% larger.

The ability to change pinholes automatically within a queue so that different resolutions can be achieved for different samples is a likely upgrade path that will require further characterization of the beamline to determine beam stability and the reproducibility of the assembly.

4. Sample environment

The sample-mounting system has been designed so that multiple samples of varying size, shape and thickness can be mounted together, all while maintaining a consistent analytical surface plane so that they all share a common alignment with the beam (Fig. 3). This greatly reduces the number of sample changeovers and the time taken for realignment of the experiment for each sample. This system consists of an aluminum frame that holds up to four aluminum breadboard

plates, to which samples can be affixed with clamps or tape. The positions of the plates can be adjusted to compensate for samples of different thicknesses.

For hard X-ray analysis, samples can be analyzed in air. For tender X-ray analysis, the presence of air results in significant attenuation of the incident beam as well as the XRF signals of important low- Z elements such as S (88% at 2307 eV in 50 mm air) and P (96% at 2013 eV in 50 mm air). Therefore, substituting air with a lighter gas such as He within an environmental chamber greatly improves the signal quality. For example, for a 50 mm beam path, He reduces the attenuation of the incident beam at 3150 eV from 57% to $\sim 0.001\%$. For beamlines that deal with smaller samples such as thin sections, this is much easier to address as the whole sample, its stages, the detector snout and the incident beam path can all be encased in a reasonably sized box or bag. However, in order to accommodate the large travel ranges and samples used in the system described here, this would be impractical requiring $\sim 3\ \text{m}^3$ to be purged of air. Therefore, we designed a system where only the sample mount is placed within a polycarbonate enclosure but not the scanning stages and the detector. The X-ray beam and the XRF facing part of the enclosure consists of a removable frame with a thin ($\sim 17\ \mu\text{m}$) commercial polypropylene film stretched across it. This allows the chamber to be purged with He while keeping attenuation of the incident X-rays to the sample surface and the fluorescence X-rays to the detector minimized. The total beam attenuation after the pinhole at the sample is $\sim 18\%$ at 3150 eV. This includes the attenuation through the polypropylene in front of the pinholes which is 5 μm thick ($\sqrt{2}\times$ thickness of polypropylene, with no air gap included in this calculation as the pinhole assembly contacts the sample window). Furthermore, in order to minimize the air path to the detector, the detector has a collimator (Fig. 2) with a 45° chamfer and a 5 μm polypropylene film that contacts the sample-chamber window

when the sample is scanned. This collimator is purged with He siphoned off from the pinhole assembly which is connected to the beam pipe He supply. The attenuation of the fluoresced X-rays by the time of incidence on the detector window is $\sim 38\%$ for S at 2307 eV and $\sim 51\%$ for P at 2013 eV.

5. Examples

An experiment typically maps a sample at an incident beam energy that promotes fluorescence of many elements of interest (e.g. 13.5 keV). This is followed by prospective XAS analyses for a specific element of interest based on features identified in the maps. Based on spectroscopy, which identifies specific resonances that correspond to different effective oxidation states, distributions of different

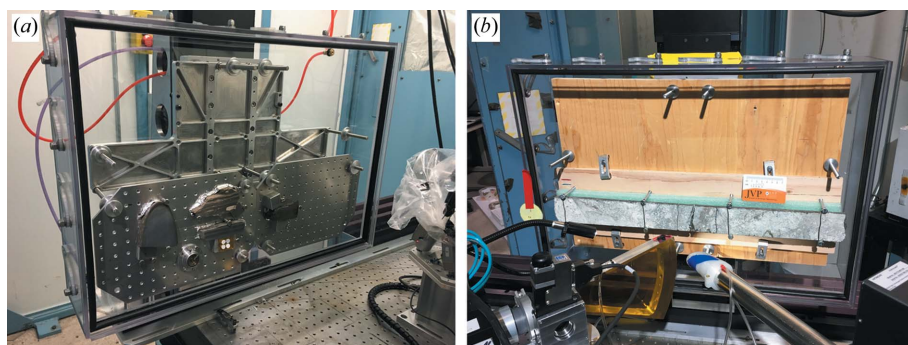


Figure 3

Photographs of the sample environment within the polycarbonate enclosure used for tender X-ray experiments; the polypropylene window was removed for clarity. (a) View of the breadboard adaptation of the sample environment designed for mounting samples of irregular shapes, in particular, allowing for samples of various thicknesses to be mounted simultaneously while maintaining a common analytical surface plane. The breadboards can be arranged in a wide number of combinations. For scale, breadboard holes are spaced at 20 mm. (b) The same sample environment adapted to hold a single large sample, in this case a 600 mm section of rock core taken from the San Andreas Fault at Elizabeth Lake in Los Angeles County, California USA, at $\sim 300\ \text{m}$ depth. In this case, the optimal solution was to use a piece of plywood with holes drilled in appropriate places to clamp the sample on.

species within a sample can be mapped in detail by performing XRF imaging at different excitation energies corresponding to those resonances. Using these ‘sparse excitation energy maps’, various statistical analyses, such as correlation plots and principal component analysis (PCA), can be quickly performed at the beamline using available software (Webb, 2011). The information from these analyses can aid in identifying statistical relationships and patterns within the data not immediately obvious just by interrogation of the concentration maps. Finally, this information can be used to identify features and regions for more targeted XAS analysis that also better represent the chemical variation within a sample.

Figs. 4 and 5 present example data collected with the instrument during the first commissioning run. Fig. 4 shows XRF images acquired from a 600 mm-long, 60 mm-diameter section of rock core through the San Andreas Fault, near Elizabeth Lake in Los Angeles County, CA, USA, at ~300 m depth. The Los Angeles Aqueduct, constructed in 1910, travels through an 8 km-long tunnel from the Mojave Desert to the Los Angeles Basin. Geotechnical investigations are ongoing to determine how to retrofit the tunnel in the case of a large earthquake rupture where the tunnel crosses the San Andreas Fault. Core from this depth allows examination of host rock that has not be affected by near-surface alteration processes.

Chemical analysis can provide crucial information as to the mineralogy and fabric of the rock deformed by the fault, and thus enable geologists to better characterize the geology of the area for engineering purposes. The lighter colored regions (Fig. 3*b*) are less deformed host rock, and dark green to gray zones are highly sheared zones likely associated with fault slip. The ability to map iron at various spatial resolutions allows examination of the nature of fluid-rock interactions and fluid flow in fractures and faults of the damage zone of the fault (Evans *et al.*, 2017).

The instrument was operated as illustrated in Fig. 1 and Fig. 3*b*), showing the core sample mounted for analysis. Fig. 4*a*) shows the Fe $K\alpha$ XRF map of almost the entire length of the core (470 mm × 214 mm) acquired at 200 μm step size with a 50 μm pinhole and 5 ms dwell time. This map took 40 min to acquire. Fig. 4*b*) shows the map of the same area acquired at 50 μm step size with 50 μm pinhole and 5 ms dwell time. This image consists of four separate maps stitched together post analysis, but these were defined and set up in a queue to run overnight. The total time to acquire this whole image (363.5 mm × 241 mm) was ~11 h 30 min (including map overlaps). Panel (c) shows the section of map acquired in the red box in panel (b), which took ~2 h 47 min to acquire (118.5 mm × 21.4 mm). Panels (d) and (e) show a magnified portion of the yellow box region in panel (a) acquired at step sizes of 200 μm and 25 μm , respectively, to illustrate the improvement in resolution. The time to acquire the total image shown in panel (e) (28.75 × 11.27 mm) was ~2 h, but only 50% of the width is shown here.

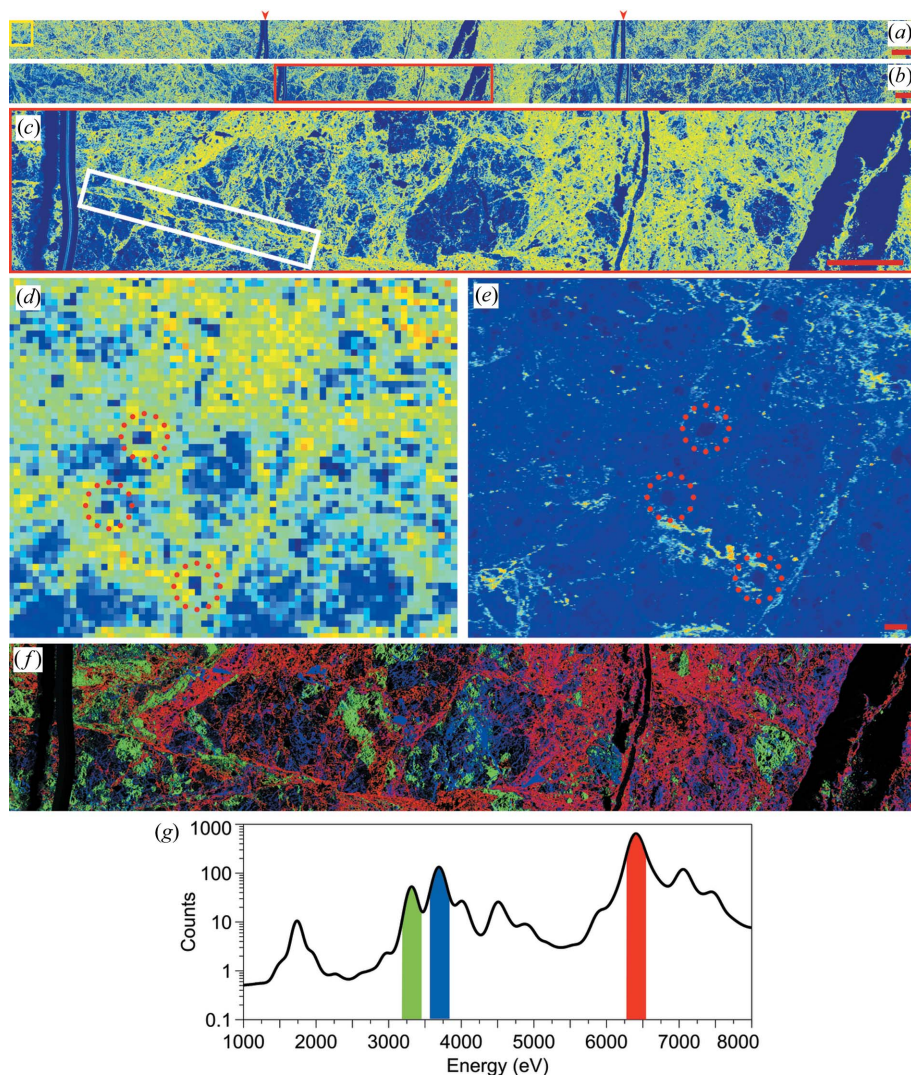


Figure 4 Iron maps taken at various pinhole apertures, all acquired with a 5 ms dwell time and a beam energy of 7500 eV. (a) 50 μm pinhole with a 200 μm step size, acquisition time ~40 min. Red arrowheads show the position of support wires seen in Fig. 3*b*). (b) 50 μm pinhole with a 50 μm step size. This map consists of four individual map sections taking an overall acquisition time of ~11 h 15 min. (c) Magnified section of the red box in (b). (d) Magnified view of the 200 μm step-size map taken from the yellow box in panel (a). (e) The corresponding area in (d) mapped with a 25 μm pinhole and a 25 μm step size. The red dotted circles mark common features in the maps. Panel (e) map acquisition time = ~2 h but the map shown is ~50% of the total map area acquired. (f) False-color composite image of Fe (red), K (green) and Ca (blue). (g) XRF spectrum average across most of the map area in (f) with the element emission peaks highlighted in the corresponding colors to the map. All scale bars in panels (a), (b) and (c) = 10 mm, panel (e) = 1 mm.

Pinhole changes were made within seconds and required no alignment optimization.

These data enable the visualization of gross rock textures and distribution of elements, and the fine-scale maps reveal distribution of elements, in this case Fe, related to shearing. Whole core images reveal that iron has been added to the fault zone (yellow *versus* blue regions), likely *via* iron-bearing fluids (Figs. 4a and 4b). The very fine-grained fault zone in the middle of the core (Figs. 4a and 4b) is enriched in iron. The higher-resolution images shows that the iron-bearing fluids were concentrated in fractures, which appear to have evolved to fault-slip surfaces in some cases [surface feature within the white box in panel (c)].

The subtle shade differences seen in panel (e) reveal different generations of fault gouge, which with further study will allow the determination of the relative timing of the chemistry and deformation in the rock. The textures of the core from this region seen in panel (e) would be very difficult to interpret without XRF mapping as they cannot be seen *via*

optical images or scanning electron microscopy. Ongoing work examines how and why Fe is added to sheared regions relative to Fe-poor host rocks, as well as interrogating the data for further chemical evidence of fluid-flow and alteration.

Fig. 5 shows data acquired to illustrate the low-*Z* imaging and XAS capabilities of the instrument. This is a thin section of a geological sample collected from the middle interval of the Miocene Monterey Formation [MMF, Fig. 5(a) which is exposed at El Capitán beach, Santa Barbara County, California, USA (Hornafius, 1985)]. SRS-XRF elemental mapping and S XAS analyses is being coupled with bulk elemental XRF Fe analysis with the aim of elucidating the critical environmental factors governing the formation of pyrite and the sulfurization of organic matter in these (and other) economically important oil-bearing sequences (Damste & Leeuw, 1990; Van Kaam-Peters *et al.*, 1998). In this sample, sedimentary layers are conspicuous because of the color banding in the optical image of the thin section (Fig. 5a) caused by variable amounts of organic material (brown) and phosphate mineral precipitates (light color). The fine-grained nature of primary silicate minerals is easily resolved by XRF imaging (Fig. 5b) as is the phosphate enrichment in the light colored bands (Fig. 5c). Sulfur obviously correlates with the organic-rich strata (Fig. 5d). The time taken to acquire the maps in panels (b)–(d) was 2 h 32 min (38.6 mm × 22 mm). Based on spectroscopy (Fig. 5e), which identifies specific resonances that correspond to different effective oxidation states of S, the complex distributions of different S species within this important hydrocarbon-rich lithology can be mapped in detail by performing XRF imaging at different incident energies corresponding to those resonances (Figs. 5f–5i). The time taken to acquire these four energy maps was 4 h 41 min (6.6 mm × 18 mm, also see footnote for Table 1). For this specimen, Fig. 5(f) in particular shows that the organic rich areas are especially enriched in the S resonance at 2473.6 eV.

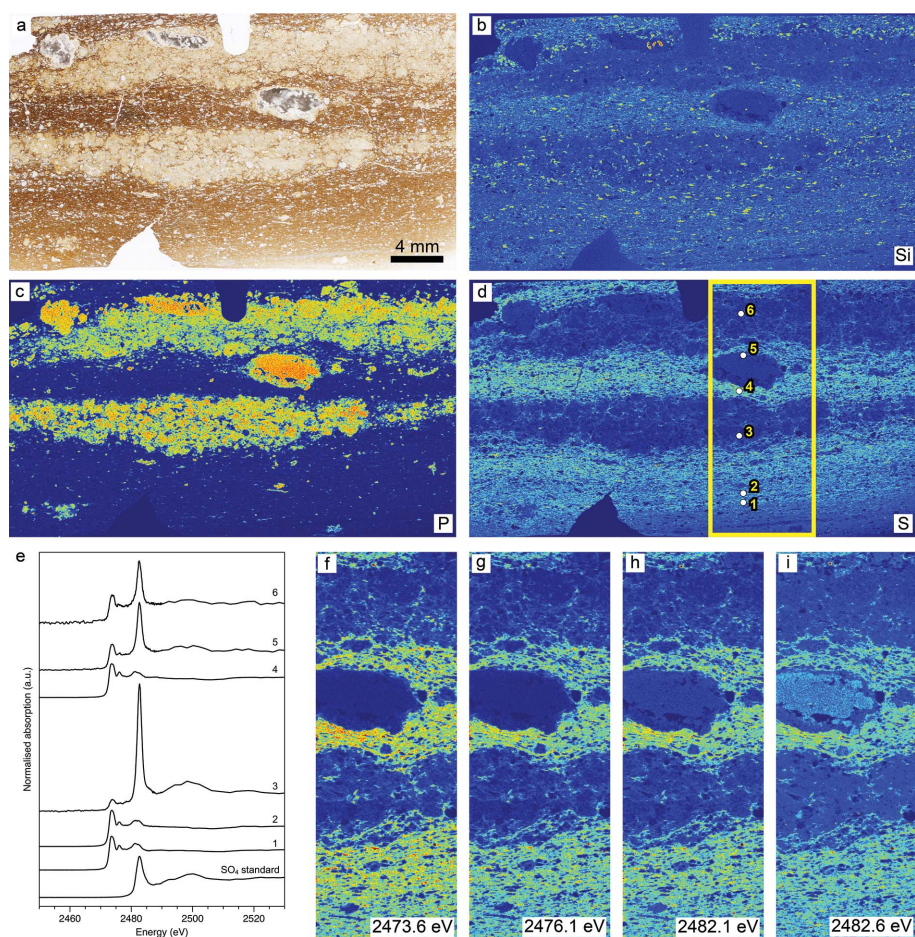


Figure 5

Tender X-ray imaging and S XAS of a thin section of Monterey Formation (a). Panels (b), (c) and (d) show the XRF maps of Si, P and S, respectively, acquired with an incident beam energy of 2560 eV, a 35 μm pinhole and 5 ms dwell time. Numbered points in panel (d) show locations of S XANES corresponding to the numbered spectra in panel (e). A sulfate standard is shown for reference. Panels (f)–(i) show maps taken from the region in the yellow box in panel (d) with incident beam energies corresponding to S XANES resonances present in panel (e). All map intensities scaled from 0 to 250 counts.

A set of scan times from commissioning runs is presented in Table 1. Note that there is currently a time overhead per line, mostly deriving from data readout and data saving, which has to be completed before the next scan line starts. As the Xpress3 system was initially designed for small scan areas (a few millimeters wide), data readout/saving speed was relatively inconsequential and negligible compared with the map width. As we have applied

Table 1

Map parameters and corresponding scan times (map sizes rounded to nearest millimeter unless otherwise indicated).

There is an overhead per line while data are read out and saved as indicated by the difference in theoretical time (simply dwell time \times No. of pixels)

Width (mm)	Height (mm)	Dwell (ms)	Step (μm)	No. of pixels	Theoretical time (HR:MIN:SEC)	Actual time (HR:MIN)
29	11	5	25	518650	0:43:13	2:08
112	678	5	50	3023757	4:11:59	8:00
130	35	5	50	1820000	2:31:40	4:01
160	21	5	50	1344000	1:52:00	3:20
280	200	5	150	2488889	3:27:24	7:50
280	200	5	120	3888889	5:24:04	10:13
280	200	3	100	5600000	4:40:00	13:23
470	21.4	5	200	251450	0:20:57	0:40
38.6	22	5	35	689286	0:57:26	2:32
6.6†	18	5	35	96980	0:32:20	4:41

† This was the multiple sulfur energy maps presented in Fig. 5 panels (f)–(i). The No. of pixels value shown is for one energy map. The theoretical and actual times stated are those to complete all four energy maps. The large overhead here can be mainly attributed to the monochromator moving to each energy at each line. In this system, rather than acquiring the full map area one energy at a time, every energy defined by the user is acquired for each line. Although this may take longer overall, it provides a safeguard against data loss (such as a beam dump) as a full set of energies is acquired for whatever portion of the region has been completed, rather than having the full region mapped for an incomplete set of energies.

this to larger areas, we have found that the overhead has a greater impact on the overall scan time. We are investigating ways of reducing this overhead which will come mostly through software development.

6. Conclusions

Described here is a large-range continuous rapid-scan XRF imaging station at the SSRL at SLAC National Accelerator Laboratory that incorporates the latest in detector and signal processing components.

The station has a scan range of 1000 mm \times 600 mm, a load capacity of up to 25 kg and is currently capable of 25–100 μm resolution elemental XRF mapping and XAS of a wide range of materials. The sample environment allows multiple specimens to be mounted at the same time, reducing the number of sample changes. The control software also allows a series of maps or XAS analyses to be queued, which also reduces the attendance time required at the beamline.

The instrument is operable in the commissioning stage and will continue to be developed. Beam spot sizes $<10 \mu\text{m}$ will be possible with a poly-capillary or an axially symmetric achromatic optic (budget dependent) and will be part of the multi-pinhole assembly discussed above. The hexapod was installed specifically in preparation of this optic which requires the versatility of six-axis motion for alignment.

This instrument provides a unique set of capabilities compared with instruments at other synchrotron facilities, in particular, the ability to image elements such as S on a decimeter scale. The scientific community has shown a growing interest in large scale combined XRF and XAS imaging and it is hoped that the versatility of this new station will contribute greatly to scientific discoveries in multiple research fields.

Acknowledgements

We thank all the support staff at SSRL, particularly Ross Arthur who designed and fabricated the sample chamber and pinhole mechanisms described here, and David Day. We also thank Professor James P. Evans, Department of Geology, Utah State University, Logan, USA, for use of the data presented in Fig. 4. We gratefully acknowledge permission from Yusuf Abubakar (PhD student at the University of Manchester, UK, funded by the Petroleum Technology Development Fund, Nigeria, award number 16PhD153) to present the data in Fig. 5.

Funding information

Funding for the SSRL 6-2 instrument was provided by the Bruce Leak and Sandra Fairon Stanford PULSE Institute Fund. Partial funding for NPE was made available by the UK EPSRC funding council under the Innovate programme. PLM acknowledges STFC for their support (ST/M001814/1). Professor Evans's work is supported by grants from the Southern California Earthquake Center and the National Science Foundation. Use of the Stanford Synchrotron Radiation Lightsource, SLAC National Accelerator Laboratory, is supported by the US Department of Energy, Office of Science, Office of Basic Energy Sciences under Contract No. DE-AC02-76SF00515. The SSRL Structural Molecular Biology Program is supported by the DOE Office of Biological and Environmental Research, and by the National Institutes of Health, National Institute of General Medical Sciences (including P41GM103393). The contents of this publication are solely the responsibility of the authors and do not necessarily represent the official views of NIGMS or NIH.

References

- Anné, J., Wogelius, R. A., Edwards, N. P., van Veelen, A., Ignatyev, K. & Manning, P. L. (2016). *Metallomics*, **8**, 508–513.
- Anné, J., Edwards, N. P., van Veelen, A., Egerton, V. M., Manning, P. L., Mosselmans, J. F. W., Parry, S., Sellers, W. I., Buckley, M. & Wogelius, R. A. (2017). *J. Anal. At. Spectrom.* **32**, 967–974.
- Anné, J., Edwards, N. P., Wogelius, R. A., Tumarkin-Deratzian, A. R., Sellers, W. I., van Veelen, A., Bergmann, U., Sokaras, D., Alonso-Mori, R., Ignatyev, K., Egerton, V. M. & Manning, P. L. (2014). *J. R. Soc. Interface*, **11**, 20140277.
- Aquilanti, G. (2015). *Synchrotron Radiation: Basics, Methods and Applications*, edited by S. Mobilio, F. Boscherini and C. Meneghini, pp. 65–104. Berlin, Heidelberg: Springer.
- Barkan, S., Saveliev, V. D., Wang, Y., Feng, L., Zhang, M., Damron, E. V. & Tomimatsu, Y. (2015). *Biol. Chem. Res.* **2015**, 338–344.
- Bergmann, U. (2007). *Phys. World*, **20**, 39–42.
- Bergmann, U., Manning, P. L. & Wogelius, R. A. (2012). *Annu. Rev. Anal. Chem.* **5**, 361–389.

- Bergmann, U., Morton, R. W., Manning, P. L., Sellers, W. I., Farrar, S., Huntley, K. G., Wogelius, R. A. & Larson, P. (2010). *Proc. Natl Acad. Sci. USA*, **107**, 9060–9065.
- Bertrand, L., Robinet, L., Thoury, M., Janssens, K., Cohen, S. X. & Schöder, S. (2012). *Appl. Phys. A*, **106**, 377–396.
- Brown, G. E. & Sturchio, N. C. (2002). *Rev. Mineral. Geochem.* **49**, 1–115.
- Diaz-Moreno, S., Amboage, M., Basham, M., Boada, R., Bricknell, N. E., Cibir, G., Cobb, T. M., Filik, J., Freeman, A., Geraki, K., Gianolio, D., Hayama, S., Ignatyev, K., Keenan, L., Mikulska, I., Mosselmans, J. F. W., Mudd, J. J. & Parry, S. A. (2018). *J. Synchrotron Rad.* **25**, 998–1009.
- Dooryhée, E., Martinetto, P., Walter, P. & Anne, M. (2004). *Radiat. Phys. Chem.* **71**, 863–868.
- Edwards, N. P., Manning, P. L., Bergmann, U., Larson, P. L., van Dongen, B. E., Sellers, W. I., Webb, S. M., Sokaras, D., Alonso-Mori, R., Ignatyev, K., Barden, H. E., van Veelen, A., Anné, J., Egerton, V. M. & Wogelius, R. A. (2014). *Metallomics*, **6**, 774–782.
- Edwards, N. P., van Veelen, A., Anné, J., Manning, P. L., Bergmann, U., Sellers, W. I., Egerton, V. M., Sokaras, D., Alonso-Mori, R., Wakamatsu, K., Ito, S. & Wogelius, R. A. (2016). *Sci. Rep.* **6**, 34002.
- Egerton, V. M., Wogelius, R. A., Norell, M. A., Edwards, N. P., Sellers, W. I., Bergmann, U., Sokaras, D., Alonso-Mori, R., Ignatyev, K., van Veelen, A., Anné, J., van Dongen, B., Knoll, F. & Manning, P. L. (2015). *J. Anal. At. Spectrom.* **30**, 627–634.
- Evans, J. P., Lindvall, S., Kerwin, S., Ballard, C., Williams, R. T., Bradbury, K. K., Tyson, J., Rowe, C. D. & Savage, H. M. (2017). *Geological Society of American Annual Meeting*. Seattle, Washington, USA.
- Gueriau, P., Jauvion, C. & Mocuta, C. (2018). *Palaeontology*, doi:10.1111/pala.12377.
- Harazim, D., McIlroy, D., Edwards, N. P., Wogelius, R. A., Manning, P. L., Poduska, K. M., Layne, G. D., Sokaras, D., Alonso-Mori, R. & Bergmann, U. (2015). *Geology*, **43**, 1007–1010.
- Hornafius, J. S. (1985). *J. Geophys. Res. Solid Earth*, **90**, 12503–12522.
- Janssens, K., Alfeld, M., Van der Snickt, G., De Nolf, W., Vanmeert, F., Radepon, M., Monico, L., Dik, J., Cotte, M., Falkenberg, G., Miliani, C. & Brunetti, B. G. (2013). *Annu. Rev. Anal. Chem.* **6**, 399–425.
- Johnson, J. E., Webb, S. M., Ma, C. & Fischer, W. W. (2016). *Geochim. Cosmochim. Acta*, **173**, 210–231.
- Kempson, I., Smith, E., Gao, M., de Jonge, M. & Thierry, B. (2014). *J. Instrum.* **9**, C12040.
- Kirkham, R., Dunn, P. A., Kuczewski, A. J., Siddons, D. P., Dodanwala, R., Moorhead, G. F., Ryan, C. G., De Geronimo, G., Beuttenmuller, R., Pinelli, D., Pfeffer, M., Davey, P., Jensen, M., Paterson, D. J., de Jonge, M. D., Howard, D. L., Küsel, M., McKinlay, J., Garrett, R., Gentle, I., Nugent, K. & Wilkins, S. (2010). *AIP Conf. Proc.* **1234**, 240–243.
- Korbas, M., Blechinger, S. R., Krone, P. H., Pickering, I. J. & George, G. N. (2008). *Proc. Natl Acad. Sci. USA*, **105**, 12108–12112.
- Lanzirotti, A., Newville, M., Manoukian, L., Lange, K., Schäfer, T., Dohrmann, R. & Greenwell, H. (2016). *Clay Clay Miner.* **21**, 53–64.
- Paterson, D., de Jonge, M. D., Howard, D. L., Lewis, W., McKinlay, J., Starritt, A., Kusel, M., Ryan, C. G., Kirkham, R., Moorhead, G., Siddons, D. P., McNulty, I., Eyberger, C. & Lai, B. (2011). *AIP Conf. Proc.* **1365**, 219–222.
- Popescu, B. F. G., George, M. J., Bergmann, U., Garachtchenko, A. V., Kelly, M. E., McCrea, R. P. E., Lüning, K., Devon, R. M., George, G. N., Hanson, A. D., Harder, S. M., Chapman, L. D., Pickering, I. J. & Nichol, H. (2009). *Phys. Med. Biol.* **54**, 651–663.
- Punshon, T., Guerinot, M. L. & Lanzirotti, A. (2009). *Ann. Bot.* **103**, 665–672.
- Sandström, M., Jalilehvand, F., Damian, E., Fors, Y., Gelius, U., Jones, M. & Salomé, M. (2005). *Proc. Natl Acad. Sci. USA*, **102**, 14165–14170.
- Sinninghe Damste, J. S. & De Leeuw, J. W. (1990). *Org. Geochem.* **16**, 1077–1101.
- Sokaras, D., Weng, T. C., Nordlund, D., Alonso-Mori, R., Velikov, P., Wenger, D., Garachtchenko, A., George, M., Borzenets, V., Johnson, B., Rabedeau, T. & Bergmann, U. (2013). *Rev. Sci. Instrum.* **84**, 053102.
- Suortti, P. & Thomlinson, W. (2003). *Phys. Med. Biol.* **48**, R1–R35.
- Templeton, A. & Knowles, E. (2009). *Annu. Rev. Earth Planet. Sci.* **37**, 367–391.
- Van Kaam-Peters, H. M. E., Schouten, S., Köster, J. & Sinninghe Damstè, J. S. (1998). *Geochim. Cosmochim. Acta*, **62**, 3259–3283.
- Vogt, S. & Lanzirotti, A. (2013). *Synchrotron Radiat. News*, **26**, 32–38.
- Webb, S. (2011). *The MicroAnalysis Toolkit: X-ray Fluorescence Image Processing Software*. SLAC National Accelerator Laboratory, CA, USA.
- Wiedemann, H. (2003). *Synchrotron Radiation*. Berlin, Heidelberg, New York: Springer-Verlag.
- Winick, H. (1994). *Synchrotron Radiation Sources: A Primer*. Singapore: World Scientific.
- Wogelius, R., Manning, P. L., Barden, H. E., Edwards, N. P., Webb, S. M., Sellers, W. I., Taylor, K. G., Larson, P. L., Dodson, P., You, H., Da-qing, L. & Bergmann, U. (2011). *Science*, **333**, 1622–1626.
- Zielińska, A., Dąbrowski, W., Fiutowski, T., Mindur, B., Wiącek, P. & Wróbel, P. (2013). *J. Instrum.* **8**, P10011.